

Vacancy-Induced Quantum Properties in 2D Silicon Carbide: Atomistic insights from semi-local and hybrid DFT calculations

Abhirup Patra^{1,2,*}

¹*Department of Chemical and Biomedical Engineering*

²*Delaware Energy Institute, University of Delaware
221 Academy St, Newark, DE 19711, USA*

Two-dimensional (2D) materials have emerged as promising platforms for quantum technologies and optoelectronics, with defects playing a crucial role in their properties. We present a comprehensive density functional theory study of silicon and carbon vacancies in monolayer silicon carbide (1L-SiC), a wide-bandgap 2D semiconductor with potential for room-temperature quantum applications. Using PBE, SCAN, r²SCAN, and HSE06 functionals, we reveal distinct characteristics between Si and C vacancies. Formation energies and charge transition levels show strong functional dependence, with HSE06 consistently predicting higher values and deeper transition levels compared to PBE calculations. Electronic structure analysis demonstrates contrasting behavior: silicon vacancies create highly localized states with strong spin polarization, while carbon vacancies produce more dispersed states with weaker magnetic properties. Vacancy migration studies reveal significantly lower barriers for silicon vacancies compared to carbon vacancies, indicating higher mobility for Si vacancies at moderate temperatures. Optical properties, calculated using PBE-DFPT, show distinct charge-state dependent absorption in the far-infrared region, with positively charged states of both vacancy types demonstrating the strongest response. The complementary characteristics of Si and C vacancies - localized versus dispersed states, different magnetic properties, and distinct optical responses - suggest possibilities for defect engineering in quantum and optoelectronic applications. Our results highlight the critical importance of advanced functionals in accurately describing defect properties and provide a comprehensive framework for understanding vacancy behavior in 2D materials.

I. INTRODUCTION

The field of two-dimensional (2D) semiconductors has witnessed remarkable progress in recent years, driven by the discovery of novel materials and their intriguing properties. These atomically thin materials, characterized by their unique electronic and optical characteristics, have opened up exciting avenues for various applications, particularly in the realm of quantum information science and optoelectronics. Among the prominent 2D semiconductors, silicon carbide (SiC) has emerged as a promising candidate due to its exceptional quantum properties at room temperature. Defects within SiC, such as silicon vacancies (V_{Si}) and carbon antisites (Si_C), play a pivotal role in enabling single-photon emission, a crucial aspect of quantum communications [1–3]. Through advanced spectroscopic techniques like electron spin resonance (ESR) and photoluminescence (PL), researchers have gained valuable insights into the nature of these defect states and their impact on the material’s electronic and optical properties [4–10]. While significant advancements have been made in the study of 3D SiC, exploring the two-dimensional form presents an exciting opportunity. Theoretical predictions suggest that local defects in 2D SiC could outperform their 3D counterparts in terms of photon emission efficiency [11–13]. Furthermore, the existence of Stone-Wales defects, created by rotating a carbon-carbon bond in the SiC lattice, has been pro-

posed, offering superior radiative transitions compared to isolated point defects [14]. Despite the promising theoretical predictions, realizing the potential of 2D SiC in practice remains a significant challenge due to difficulties in synthesizing high-quality 2D SiC and controlling defects at the atomic level [15–20]. To characterize and study the defects in 2D SiC, advanced techniques with atomic-scale resolution are essential. Scanning tunneling microscopy (STM), high-resolution transmission electron microscopy (HRTEM), and specialized optical characterization methods like photoluminescence (PL) spectroscopy have been instrumental in probing the atomic structure and properties of defects [7, 21–26]. Substantial progress has been achieved in comprehending the dynamics of defects in 2D SiC via advanced theoretical research, particularly with respect to thermodynamic stability [27–29]. First-principles calculations based on density functional theory (DFT) have provided valuable insights into the formation energies, electronic structure, and optical properties of various defects in 2D SiC. By comparing the calculated defect formation energies and charge transition levels with experimental data, researchers can identify the most stable defect configurations and predict their behavior under different environmental conditions. One notable theoretical achievement is the prediction of the stability of the divacancy-complex ($V_{Si}V_C$) in 2D SiC. DFT calculations using hybrid functionals, such as HSE06, have shown that the divacancy-complex exhibits remarkably low formation energy and is thermodynamically favorable compared to isolated vacancies [27]. This finding has important implications for experimentalists

* patraa@udel.edu

aiming to engineer and control defects in freestanding 2D SiC, as the divacancy-complex can serve as a stable and optically active center for quantum applications.

Moreover, DFT calculations have provided valuable insights into the spin-strain coupling properties of defects in 2D SiC [28]. By analyzing the electronic structure and spin density distribution of defects under different strain conditions, researchers can predict the sensitivity of defect-related optical transitions to mechanical deformation. This knowledge is crucial for developing strain-tunable quantum emitters and sensors based on 2D SiC. Recent theoretical studies have also explored the potential of defect engineering in 2D SiC through the incorporation of foreign atoms or the creation of specific defect complexes [29]. DFT calculations have predicted that doping 2D SiC with elements such as nitrogen or boron can introduce new energy levels and optical transitions, enabling the tuning of the material's electronic and optical properties. Recent experimental breakthroughs in synthesizing 2D SiC have validated many theoretical predictions about its properties and stability. Both top-down chemical exfoliation [30] and bottom-up epitaxial growth on transition metal carbides [31] have demonstrated the feasibility of producing monolayer SiC. These advances provide crucial experimental validation of the structural and electronic properties predicted by theory, while also revealing new phenomena such as strong spin-orbit coupling effects in substrate-supported 2D SiC [31]. However, the accuracy of DFT calculations hinges on the chosen exchange-correlation functional. While PBE offers an efficient description of electron localization, it often falls short in capturing the correct electronic structure and defect formation energies [32–34]. PBE tends to underestimate the band gap of semiconductors and overdelocalize the defect states, leading to an underestimation of defect formation energies and charge transition levels. This limitation can be particularly problematic for defects in wide-bandgap materials like SiC, where the accurate description of localized defect states is crucial. Alternatively, hybrid functionals like HSE06 have emerged as a more reliable choice for defect calculations in semiconductors [35–37]. By incorporating a fraction of exact exchange from Hartree-Fock theory, HSE06 can partially correct the self-interaction error and improve the description of localized defect states. HSE06 has been shown to provide accurate band gaps and defect formation energies for a wide range of semiconductor materials, including 2D SiC. However, the computational cost of HSE06 calculations is significantly higher than that of PBE, which can limit its applicability to large-scale simulations. To bridge the gap between accuracy and computational efficiency, meta-GGA functionals like SCAN and r²SCAN have been developed [38–41]. These functionals go beyond the local density approximation (LDA) and GGA by incorporating higher-order derivatives of the electron density, such as the kinetic energy density. SCAN and r²SCAN have shown promising performance in describing the electronic structure and thermodynamic properties

of a wide range of materials, including semiconductors and 2D systems. Recent studies have demonstrated that SCAN and r²SCAN can provide accurate band gaps and defect formation energies for 2D SiC, comparable to those obtained with HSE06 [40, 41]. Moreover, these functionals have been shown to correctly capture the localization of defect states and the charge transition levels, which are crucial for understanding the optical and transport properties of defects in 2D SiC. The computational cost of SCAN and r²SCAN calculations is significantly lower than that of HSE06, making them attractive options for large-scale simulations of defects in 2D materials. However, it is important to note that while meta-GGA functionals like SCAN and r²SCAN offer improved accuracy compared to PBE, they are not a universal solution for all materials and properties. In some cases, the inclusion of exact exchange through hybrid functionals like HSE06 may still be necessary to correctly describe the electronic structure and defect properties of 2D SiC. Therefore, a careful benchmarking of different functionals against experimental data and high-level theoretical methods is essential to ensure the reliability of DFT calculations for defects in 2D SiC. The objective of this research is to examine the formation energies of Si and C vacancies in bulk and monolayer SiC using various DFT functionals. The primary aim is to evaluate the effectiveness of each functional in representing localized defect states and to comprehend the impact of these states on the material's quantum characteristics. The study aims to provide valuable insights into the theoretical basis of SiC's defects and aid in selecting appropriate computational strategies in the rapidly expanding field of SiC-based technologies. We will delve into the electronic structures of these defects and establish a correlation between their fundamental electronic properties and emerging quantum features. The ensuing sections will present the findings of this study, covering the defect formation energies (Fig. 1), electronic structure (Fig. 3), vacancy migration (Fig. 5), and optical properties (Fig. 6) of silicon and carbon vacancies in monolayer SiC.

II. COMPUTATIONAL METHODS

We conducted spin-polarized DFT calculations using the Vienna Ab initio Simulation Package (VASP) [42] with plane-wave basis sets, PAW-PBE pseudopotentials [43], and an energy cutoff of 450 eV. We employed the Generalized Gradient Approximation (GGA) with Perdew-Burke-Ernzerhof (PBE) [44], the strongly constrained and appropriately normed (SCAN) meta-GGA type [45] and its modified version r²SCAN [46], as well as the Heyd-Scuseria-Ernzerhof (HSE06) hybrid exchange-correlation functionals [47], including DFT-D3 van der Waals correction [48]. Complete relaxation of atomic positions and supercell dimensions was allowed using conjugate gradient optimization techniques without symmetry constraints. Force convergence criteria of 0.02 eV/Å

and total energy precision within 0.01 meV were achieved with Brillouin zone sampling on a $2 \times 2 \times 1$ Monkhorst-Pack k-point grid for structural optimizations and a denser $4 \times 4 \times 1$ grid for band structure calculations [49]. Migration pathways and diffusion barriers (E_b) of defect sites were computed using the climbing-image nudged elastic band (CI-NEB) method [50], as presented in Fig. 5. The optical properties were calculated using density functional perturbation theory (DFPT) within the PBE framework, which provides a computationally efficient approach for excited state properties while maintaining good accuracy for relative changes in optical response. The absorption coefficients (α) were computed from the complex dielectric function and are presented as percentages relative to the pristine case to facilitate direct comparison of vacancy effects. The energy range was chosen to focus on the far-infrared region (0-0.5 eV) where vacancy-induced features are most prominent. We determined vacancy defect formation energies in monolayer SiC by applying thermodynamic principles, considering carbon-rich environment. In this work, μ_{Si} is derived from diamond silicon, while μ_C is calculated from bulk graphite. These calculations provide insight into the preference for different vacancy defects under varied experimental conditions, as shown in Fig. 1. The Freysoldt, Neugebauer, and Van de Walle (FNV) [51] and Kumagai & Oba (KO) [52] methods are used to correct for electrostatic interactions in the calculation of defect formation energies in charged systems. The formation energies of defects in charge-state q were calculated using the equation:

$$\Delta E_f(q) = E_{tot}(q) - E_{bulk} - \sum_A n_A \mu_A + q E_{Fermi} + E_{corr} \quad (1)$$

Here, $E_{tot}(q)$ is the total energy of the supercell containing one defect of charge state q , E_{bulk} is the total energy of the defect-free supercell, μ_A is the chemical potential of the removed atom type, N_A is the number of missing atoms, E_{Fermi} is the Fermi energy referenced to the theoretical valence band maximum (VBM) for a given functional, and E_{corr} is the correction term for electrostatic interactions between periodically repeated defects, calculated using the FNV or KO method. Freysoldt's method, which is often employed in defect calculations, addresses the spurious electrostatic interaction between periodic images of charged defects in a supercell. In this scheme, a model potential is used as the basis for canceling the long-range Coulomb interaction as well as aligning the potential with the potential of a perfect bulk crystal numerically.

$$E_{Freysoldt}^{corr} = E_f + E_{corr}(q, \epsilon, L) = E_{image} + V_{align} \quad (2)$$

where q is the charge of the defect, ϵ is the dielectric constant, and L is the supercell dimension. The correction term E_{corr} consists of two parts: the alignment

of the potential, ΔV , and the image charge correction, which is a function of the charge q , the dielectric constant ϵ , and the supercell size L . The potential alignment term ensures that the defect level aligns with the bulk level far from the defect. Physically, this method acknowledges that the potential due to a charged defect should not differ from the perfect crystal at a sufficiently large distance. This aligns the electrostatic potential outside the defect region with that of the bulk, ensuring that the calculated defect formation energy reflects the intrinsic energy without artificial stabilization from periodic images. On the other hand, the Kumagai method extends the Freysoldt approach by including the anisotropic nature of the dielectric response. It uses the full dielectric tensor and computes the potential alignment term using anisotropic dielectric models, which is crucial for materials with directional bonding, such as SiC.

$$E_{Kumagai}^{corr} = E_f + E_{corr}(q, \epsilon_{ani}, L) = E_{image,ani} + V_{align,ani} \quad (3)$$

The anisotropic dielectric constant ϵ_{ani} replaces the isotropic ϵ used in Freysoldt's method. The corrected formation energy takes into account the varying dielectric response depending on the direction relative to the crystal axes. Here, $E_{image,ani}$ and $V_{align,ani}$ are computed considering the full tensor, which reflects the anisotropic electronic screening response of the material. The optical properties were calculated using density functional perturbation theory (DFPT) within the PBE framework, which provides a computationally efficient approach for excited state properties while maintaining good accuracy for relative changes in optical response. The absorption coefficients (α) were computed from the complex dielectric function (ϵ) and are presented as percentages relative to the pristine case to facilitate direct comparison of vacancy effects. The energy range was chosen to focus on the far-infrared region (0-0.5 eV) where vacancy-induced features are most prominent.

III. RESULTS AND DISCUSSION

A. Defect Formation Energies

Figure 1 presents a comprehensive analysis of vacancy formation energies in monolayer SiC (1L-SiC) under carbon-rich conditions, revealing the complex interplay between defect type, charge state, and computational methodology. The formation energies are plotted as a function of the Fermi level for both silicon vacancies (Fig. 1a) and carbon vacancies (Fig. 1b), calculated using four different exchange-correlation functionals (PBE, SCAN, r^2 SCAN, and HSE06) and two charge correction schemes: the Freysoldt-Neugebauer-Van de Walle (FNV) method (dashed lines) and the Kumagai-Oba (KO) method (solid lines). For silicon vacancies (Fig. 1a), the formation energies at the valence band maximum (VBM) exhibit a

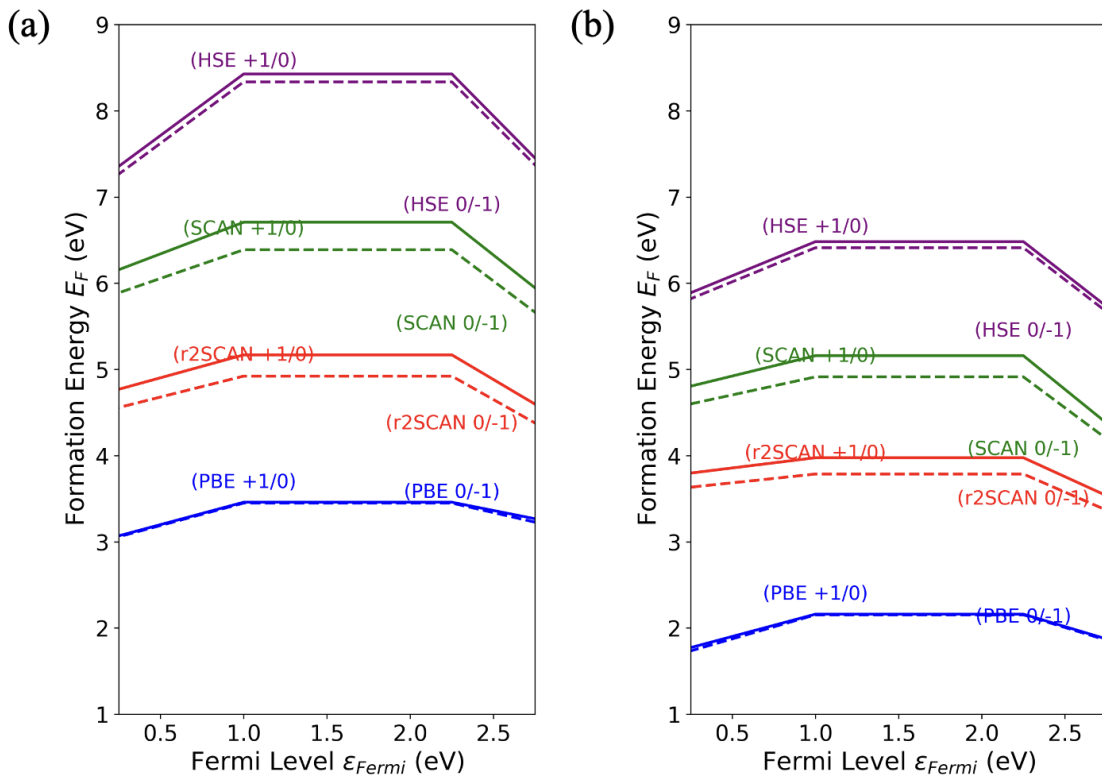


FIG. 1. Comparison of defect formation energies for (a) mono-Si vacancy and (b) C vacancy in C-rich environments. The FNV charge correction scheme results are displayed by the dashed line, while the KO charge correction scheme results are shown by the solid line. The range of Fermi levels is calculated based on the thermodynamic stability region in C-rich conditions.

significant functional dependence, ranging from approximately 4.0 eV for PBE to 7.5 eV for HSE06. This substantial variation of 3.5 eV underscores the critical role of exact exchange in accurately capturing the energetics of defect formation in semiconductors. The PBE functional, being a GGA method, tends to underestimate formation energies due to its tendency to overdelocalize electronic states. This underestimation can lead to an overestimation of defect concentrations in equilibrium conditions. In contrast, the HSE06 hybrid functional, which includes a fraction of exact exchange, provides the highest formation energies, likely offering the most accurate representation of the defect energetics. The meta-GGA functionals SCAN and r²SCAN yield intermediate results, with formation energies of about 6.0 eV and 6.5 eV respectively, reflecting their improved treatment of electron correlation compared to PBE. The progression from PBE to HSE06 demonstrates a systematic increase in formation energy, indicating that more sophisticated treatments of exchange and correlation tend to stabilize the perfect crystal relative to the defective one. As the Fermi level increases towards the conduction band minimum (CBM), the formation energies of silicon vacancies decrease steeply for all functionals, suggesting a high sensitivity to the electronic environment. This steep decrease indicates that silicon vacancies become more favorable

under n-type conditions. The slope of this decrease is particularly pronounced for the HSE06 functional, dropping by approximately 2.5 eV over a 1 eV increase in Fermi level. This behavior suggests that silicon vacancies could act as compensating defects in heavily n-doped 1L-SiC, potentially limiting the achievable electron concentrations. The charge transition levels for silicon vacancies show a clear functional dependence. The +1/0 transition occurs at 0.9 eV (PBE), 1.4 eV (r²SCAN), 1.6 eV (SCAN), and 1.8 eV (HSE06) above the VBM. Similarly, the 0/-1 transition is predicted at 1.6 eV (PBE), 2.1 eV (r²SCAN), 2.3 eV (SCAN), and 2.6 eV (HSE06) above the VBM. These differences stem from the varying abilities of the functionals to describe localized states and charge transitions accurately, with HSE06 consistently predicting the deepest transition levels. The spread of 0.9 eV for the +1/0 transition and 1.0 eV for the 0/-1 transition across functionals highlights the importance of the choice of functional in predicting the electronic properties of defects. The deep nature of these transition levels, particularly as predicted by HSE06, suggests that silicon vacancies could act as deep donor and acceptor states in 1L-SiC, potentially influencing carrier recombination and trapping processes. Carbon vacancies (Fig. 1b) consistently demonstrate lower formation energies than silicon vacancies across all functionals, ranging

from 3.0 eV for PBE to 6.0 eV for HSE06 at the VBM. This difference of 1.0-1.5 eV in formation energy compared to silicon vacancies is related to the weaker C-C bonds compared to Si-C bonds, making carbon vacancy formation energetically more favorable. The functional dependence follows a similar pattern to that observed for silicon vacancies, with PBE yielding the lowest formation energies and HSE06 the highest. The spread of 3.0 eV between PBE and HSE06 for carbon vacancies is slightly smaller than for silicon vacancies, possibly indicating a lesser degree of electron localization in carbon vacancy states. Interestingly, carbon vacancies exhibit a less steep decrease in formation energy with increasing Fermi level compared to silicon vacancies, suggesting a lower sensitivity to the electronic environment. For instance, the HSE06 formation energy drops by only about 1.5 eV over a 1 eV increase in Fermi level, compared to 2.5 eV for silicon vacancies. This behavior implies that carbon vacancies might be less effective as compensating defects in n-type material compared to silicon vacancies. The charge transition levels for carbon vacancies occur at higher Fermi level positions compared to silicon vacancies. The +1/0 transition is predicted at 1.1 eV (PBE), 1.6 eV (r^2 SCAN), 1.8 eV (SCAN), and 2.1 eV (HSE06) above the VBM. The 0/-1 transition shows a similar progression: 2.4 eV (PBE), 2.8 eV (r^2 SCAN), 3.0 eV (SCAN), and 3.2 eV (HSE06) above the VBM. The higher position of these levels compared to silicon vacancies suggests that carbon vacancies might act as deeper donor and acceptor states, potentially playing a more significant role in carrier trapping and recombination processes, especially in the mid-gap region. A comparison of the KO and FNV charge correction schemes reveals consistent differences across all functionals for both vacancy types. The KO method generally yields lower formation energies for charged defects, with the difference being most pronounced for HSE06 calculations, reaching up to 0.5 eV for negatively charged vacancies. This discrepancy underscores the importance of considering anisotropic dielectric responses in 2D materials, where reduced dimensionality leads to significant dielectric anisotropy. The KO method's ability to account for this anisotropy makes it particularly suitable for defect calculations in 2D systems, although the choice between KO and FNV can still impact quantitative predictions. The magnitude of this correction (up to 0.5 eV) is significant compared to the differences between functionals, highlighting the importance of appropriate charge corrections in 2D defect calculations. The range of Fermi levels shown in Figure 1 is based on the thermodynamic stability region in carbon-rich conditions, spanning from the VBM to approximately 2.5 eV above it for silicon vacancies and 3.0 eV for carbon vacancies. This choice of chemical potential affects the absolute values of formation energies but not the charge transition levels. The wider range for carbon vacancies suggests a broader range of stable charge states under varying electronic conditions.

B. Electronic Properties

The electronic band structure of pristine monolayer silicon carbide (1L-SiC) provides fundamental insights into its electronic properties and potential applications. Figure 2 presents a comprehensive comparison of the band structures calculated using four different DFT-XC approaches: PBE, SCAN, r^2 SCAN, and HSE06. All four functionals consistently predict that 1L-SiC is an indirect bandgap semiconductor, with the valence band maximum (VBM) located at the K-point and the conduction band minimum (CBM) at the M-point of the Brillouin zone. The calculated HSE06 bandgap of 3.39 eV is lower than the previous GW-GGA predictions (3.90 eV) of monolayer SiC [53] and in very good agreement with the HSE06 values of 3.35 eV from [54] and 3.58 eV [55]. The indirect nature of the bandgap is a key feature of 1L-SiC, distinguishing it from other 2D materials like graphene or monolayer transition metal dichalcogenides, and has important implications for its optical and electronic properties. The indirect bandgap in 1L-SiC necessitates phonon assistance for optical transitions to conserve momentum. This three-particle process (electron, hole, and phonon) is less probable than the two-particle process in direct bandgap materials, leading to longer radiative lifetimes. The phonon involvement allows the system to remain in the excited state for a longer duration, as the electron must wait for an appropriate phonon to assist in the recombination process. This mechanism can be advantageous for applications requiring sustained excited states, such as in certain photocatalytic processes or in devices exploiting long-lived excitons. Notably, the spin-up (pink) and spin-down (blue) bands are perfectly degenerate for the pristine case across all functionals, indicating the absence of any intrinsic magnetic moment in the unperturbed 1L-SiC lattice. This spin degeneracy is expected for a non-magnetic semiconductor and serves as a baseline for understanding the spin-polarized states that emerge when defects are introduced. The band dispersion characteristics show remarkable qualitative similarity across all functionals, with some quantitative differences. The valence bands exhibit strong dispersion near the K-point, particularly evident in the topmost valence band. This strong dispersion indicates high hole mobility in the K-point region, suggesting that hole transport could play a significant role in the electronic properties of p-type or ambipolar 1L-SiC devices. In contrast, the conduction bands show noticeably less dispersion, especially near the CBM at the M-point. This flatter conduction band suggests lower electron mobility compared to hole mobility, an asymmetry that could have important implications for charge transport in 1L-SiC-based devices. The lower electron mobility might result in longer electron lifetimes, which could be advantageous for applications requiring sustained electron excitation, such as in photocatalysis or certain optoelectronic devices. While the overall band structure features are consistent across functionals, there are significant quanti-

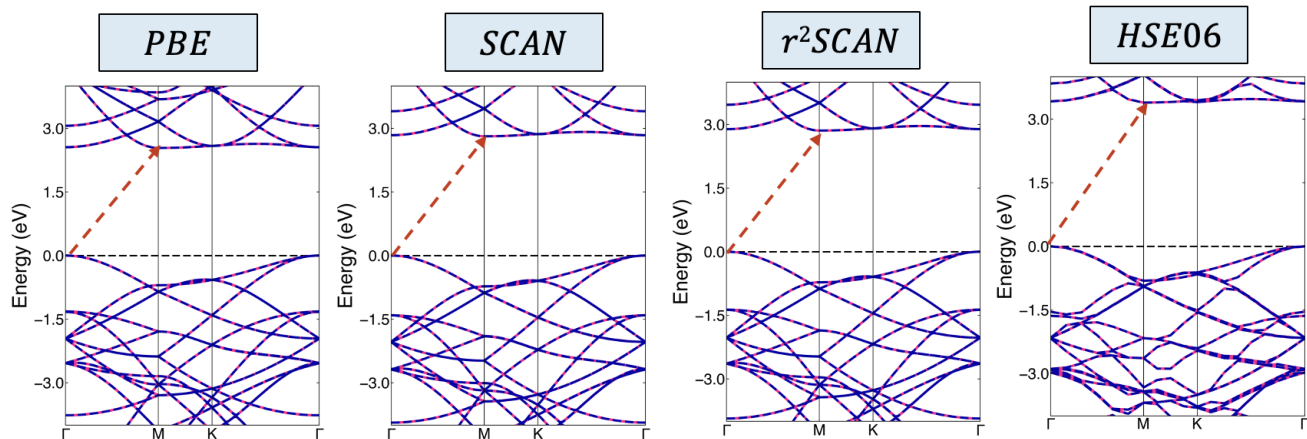


FIG. 2. Electronic band structures of pristine SiC monolayer calculated using PBE, SCAN, r^2 SCAN, and HSE functionals (from left to right). The Fermi level is set to zero.

DFT	Bandgap (eV)	Workfunction (eV)	Electron Affinity (eV)	Ionization Energy (eV)
PBE	2.54	4.85	2.46	5.10
SCAN	2.81	4.99	2.36	5.29
r^2 SCAN	2.86	5.03	2.31	5.28
HSE	3.39	4.79	2.47	5.03

TABLE I. Properties of pristine SiC monolayer computed using DFT functionals.

tative differences, particularly in the predicted bandgap values. Table I provides a comprehensive summary of key electronic properties calculated using each functional, offering valuable insights into these differences. The PBE functional, employing the GGA, predicts the smallest bandgap of 2.54 eV in good agreement with [54, 56]. This underestimation is a well-known limitation of GGA functionals, stemming from their approximate treatment of exchange-correlation effects and the lack of proper self-interaction correction. Moving to more sophisticated functionals, we observe a systematic increase in the predicted bandgap. The SCAN functional, a meta-GGA approach, yields a larger bandgap of 2.81 eV, while its refined version, r^2 SCAN, predicts a slightly higher value of 2.86 eV. This trend reflects the improved treatment of exchange-correlation effects in meta-GGA functionals, which incorporate the kinetic energy density to better account for electron localization effects. The HSE06 hybrid functional, which includes a fraction of exact exchange, predicts the largest bandgap of 3.39 eV. Beyond the bandgap, Table I reveals interesting trends in other electronic properties. The work function, a critical parameter for understanding electron emission and interface properties, shows less variation across functionals compared to the bandgap. PBE predicts a work function of 4.85 eV, while SCAN and r^2 SCAN predict slightly higher values of 4.99 eV and 5.03 eV, respectively. Interestingly, HSE06 predicts a slightly lower work function of 4.79 eV. The electron affinity, which measures the en-

ergy required to add an electron to the neutral system, shows a non-monotonic trend across functionals. PBE and HSE06 predict similar values (2.46 eV and 2.47 eV, respectively), while SCAN and r^2 SCAN predict lower values (2.36 eV and 2.31 eV). This suggests that meta-GGA functionals predict a lower tendency for 1L-SiC to accept electrons compared to both PBE and HSE06. The ionization energy follows a different pattern, with SCAN and r^2 SCAN predicting the highest values (5.29 eV and 5.28 eV), while PBE and HSE06 predict lower values (5.10 eV and 5.03 eV). These differences in electron affinity and ionization energy could significantly influence the material's chemical reactivity, charge transfer processes, and behavior in electronic devices. The introduction of silicon vacancies in 1L-SiC induces profound changes in its electronic structure, as illustrated in Figure 3 and supported by DOS analysis in Figure S1. For the neutral vacancy V_{Si}^0 (Figure 3a), PBE predicts a metallic state with spin-degenerate bands crossing the Fermi level, corresponding to a broad, unsplit DOS peak at the Fermi energy. These bands, derived primarily from dangling bond states of neighboring carbon atoms, exhibit minimal dispersion (0.2 eV bandwidth), indicating strong spatial localization of the defect states. This localization is evidenced in the DOS by sharp peaks with full width at half maximum of approximately 0.3 eV. In contrast, SCAN and r^2 SCAN open a small indirect gap of 1.25 eV, with the VBM at the Γ point and the CBM at the M point. This gap opening reflects the improved

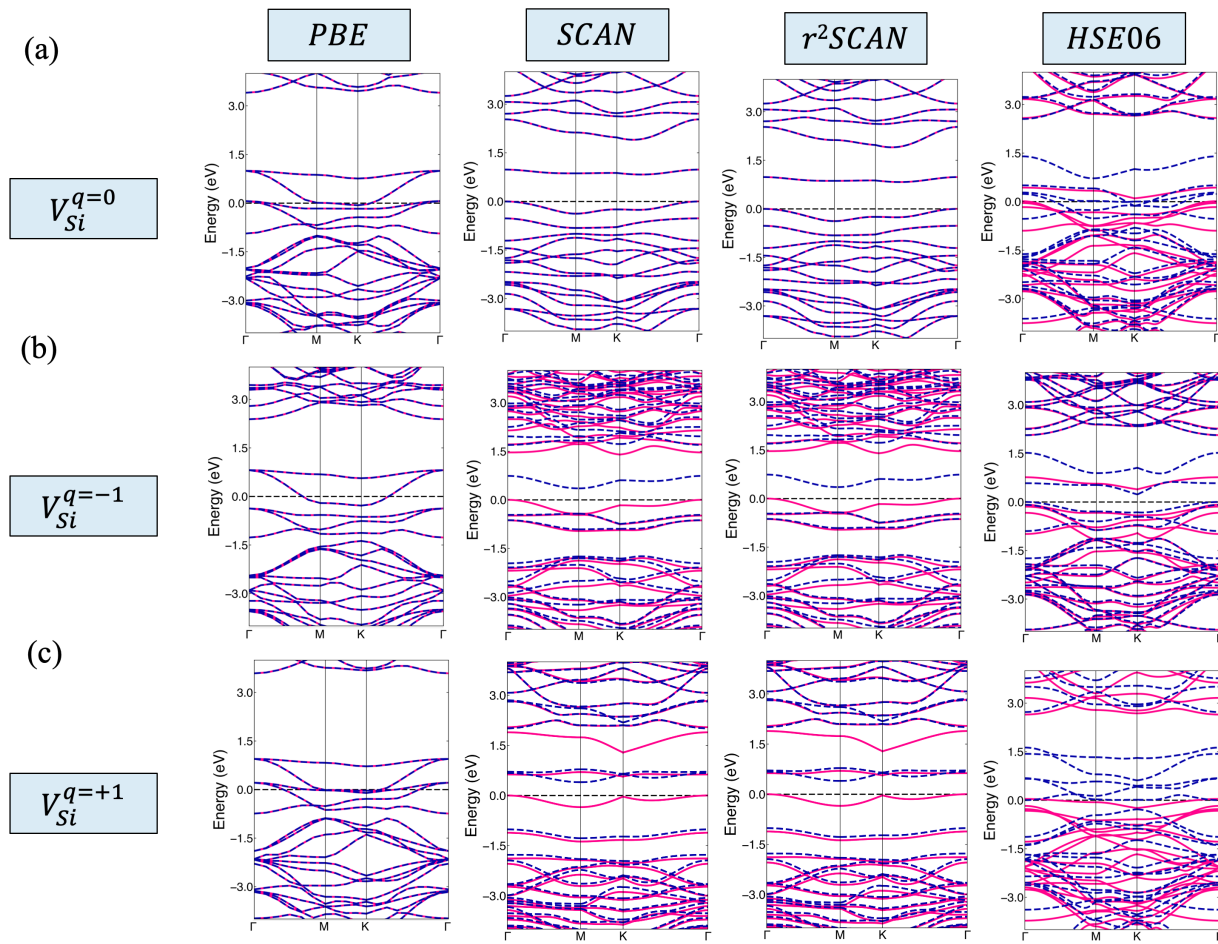


FIG. 3. Electronic band structure of the V_{Si} in a 3×3 monolayer SiC computed using PBE, SCAN, r^2 SCAN and HSE functional (with D3 dispersion correction) for the three charged vacancy states (a-c). The leftmost panel depicts the PBE, followed by SCAN, r^2 SCAN, and HSE to the right. The grey shade line depicts the band structure of a pristine SiC monolayer.

treatment of self-interaction errors in meta-GGA functionals, manifested in the DOS as a clear splitting of the defect states into occupied and unoccupied regions separated by approximately 1.25 eV. The HSE06 functional reveals a markedly different electronic structure for V_{Si}^0 . Our calculations show that the spin-up bands exhibit a gap of approximately 2.0 eV between the VBM at Γ and the CBM at K, corresponding to well-separated DOS peaks centered at -1.0 eV and +1.0 eV relative to the Fermi level. The spin-down bands, in contrast, show metallic behavior with states crossing the Fermi level, producing a sharp DOS peak at the Fermi energy with intensity approximately twice that of the spin-up peaks. This spin polarization, absent in PBE and progressively emerging in SCAN and r^2 SCAN results, demonstrates the crucial role of exact exchange in capturing the correct spin physics of localized defect states. The DOS shows a clear spin splitting of 0.7 eV between majority and minority spin channels, providing a quantitative measure of the magnetic moment. For the negatively charged silicon vacancy (V_{Si}^{-1}), shown in Figure 3b, all functionals predict more pronounced changes in the electronic struc-

ture. PBE shows increased metallicity compared to the neutral case, with multiple band crossings at the Fermi level producing a broad DOS feature spanning approximately 1 eV around the Fermi energy. This can be interpreted as the additional electron populating previously unoccupied defect states, increasing the density of states at the Fermi level. SCAN and r^2 SCAN, however, predict the opening of a gap in both spin channels, with a notable spin splitting evidenced by separated DOS peaks at -0.8 eV and +0.4 eV relative to the Fermi level. The HSE06 results for V_{Si}^{-1} exhibit the most dramatic spin polarization. A large indirect gap of 2.2 eV appears in the spin-up channel, while the spin-down channel shows a smaller gap of 0.9 eV. The DOS reveals sharply defined peaks split by 1.3 eV between spin channels, the largest spin splitting observed among all vacancy configurations. This strong spin dependence indicates that the additional electron preferentially occupies one spin channel, maximizing the exchange energy and resulting in a high-spin configuration. The DOS peaks show minimal broadening (0.2 eV width), consistent with the highly localized nature of these states. The positively

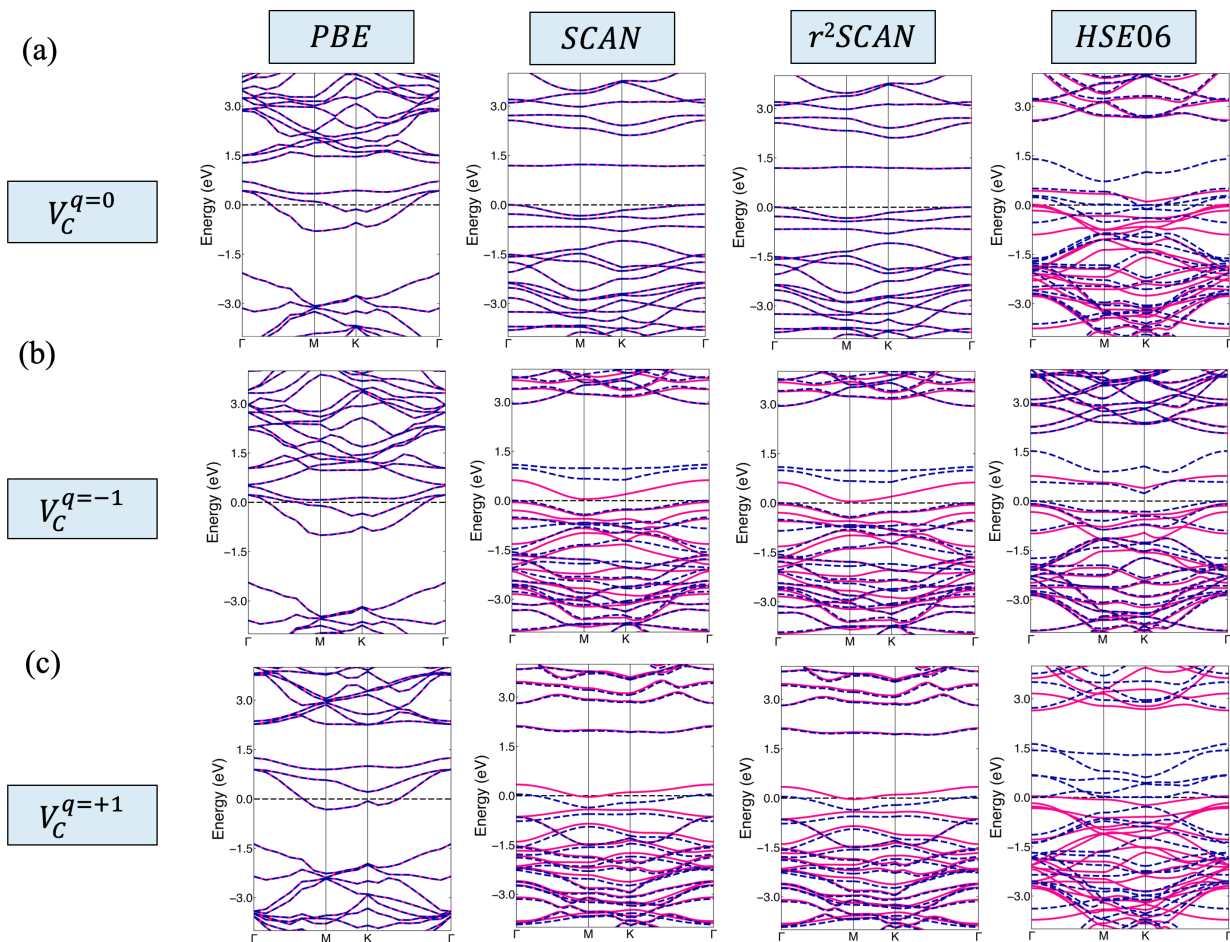


FIG. 4. Electronic band structure of the V_C in a 3×3 monolayer SiC computed using PBE, SCAN, r^2 SCAN and HSE06 functional (with D3 dispersion correction) for the three charged vacancy states (a-c). The leftmost panel depicts the PBE, followed by SCAN, r^2 SCAN, and HSE to the right. The grey shade line depicts the band structure of a pristine SiC monolayer.

charged vacancy V_{Si}^{+1} (Figure 3c) presents yet another distinct electronic landscape. PBE predicts a return to near spin degeneracy with metallic behavior, reflected in overlapping spin-up and spin-down DOS peaks at the Fermi level. SCAN and r^2 SCAN maintain some degree of spin polarization, with small spin-dependent gaps producing DOS peak splittings of 0.3-0.5 eV. The HSE06 functional, however, predicts a wide gap of 3.0 eV for spin-up states and metallic behavior for spin-down states, creating a highly asymmetric DOS with a large gap in one spin channel and a sharp peak at the Fermi level in the other. This stark asymmetry between spin channels implies a complex redistribution of electrons upon positive charging, possibly involving significant lattice relaxation and rehybridization of surrounding atoms, as evidenced by the redistribution of DOS weight between s and p orbital contributions compared to the neutral case. The DOS orbital analysis reveals that silicon vacancy states are dominated by p-orbital contributions, with p:s peak intensity ratios exceeding 3:1 in the defect state region. This strong p-orbital character per-

sists across all charge states, though the relative weights shift with charging: the p-orbital contribution increases to nearly 85% in V_{Si}^{-1} but decreases to approximately 70% in V_{Si}^{+1} , reflecting charge-state-dependent changes in the local electronic structure. Carbon vacancies demonstrate distinctive electronic characteristics that significantly differ from silicon vacancies, reflecting the fundamental differences in C-Si and Si-Si bonding in the SiC lattice. For the neutral carbon vacancy (V_C^0), HSE06 calculations predict a unique electronic structure with a spin splitting of 0.3 eV, substantially smaller than the 0.7 eV observed for V_{Si}^0 . This is evidenced by both the band structure gaps (1.5 eV for spin-up and 1.2 eV for spin-down channels) and the corresponding DOS peaks separated by 0.3 eV near the Fermi level. The defect states show broader dispersion of approximately 0.5 eV across the Brillouin zone, particularly notable along the Γ -K direction, compared to the much narrower 0.2 eV dispersion observed for silicon vacancies. The DOS analysis reveals that carbon vacancy states have significant contributions from both s and p orbitals, with p-orbital

peaks showing approximately 50% greater intensity than s-orbital peaks in the energy range of -1 to 1 eV around the Fermi level. This mixed orbital character explains the enhanced band dispersion and suggests stronger hybridization with neighboring atoms compared to the predominantly p-orbital character of silicon vacancy states. The negatively charged carbon vacancy (V_C^{-1}) exhibits a complex electronic structure that varies significantly across functionals. PBE predicts metallic behavior with multiple band crossings at the Fermi level, while SCAN and r^2 SCAN reveal the emergence of small gaps (0.4-0.6 eV) in both spin channels. The HSE06 calculations demonstrate spin-split gaps of 0.8 eV and 0.5 eV for spin-up and spin-down channels respectively, notably smaller than the corresponding gaps in V_{Si}^{-1} (2.2 eV and 0.9 eV). The DOS shows three distinct peaks at -0.8 eV, -0.2 eV, and +0.3 eV relative to the Fermi level, corresponding to specific transitions in the band structure. For the positively charged state (V_C^{+1}), HSE06 calculations reveal a direct gap of 0.6 eV at the K point for the spin-up channel, while maintaining metallic character in the spin-down channel. The DOS exhibits a sharp peak at +0.4 eV above the Fermi level in the spin-down channel, with an integrated intensity approximately twice that of the neutral state peaks, indicating enhanced state density available for optical transitions. The progression of electronic structure across charge states shows systematic trends in the DOS peak positions: the main defect state peaks shift from -0.3 eV in V_C^{-1} to 0.0 eV in V_C^0 to +0.4 eV in V_C^{+1} relative to the Fermi level, demonstrating clear charge state-dependent electronic structure evolution. This detailed analysis of band structures and DOS reveals that carbon vacancies maintain moderate spin polarization (0.3-0.8 eV splittings) across charge states, but with consistently smaller magnitudes than silicon vacancies (0.7-1.3 eV splittings). The broader bandwidth of carbon vacancy states (0.5 eV vs 0.2 eV) and mixed s-p orbital character indicate fundamentally different bonding characteristics, leading to more delocalized defect states that could influence their optical and magnetic properties.

C. Migration of Vacancies

Figure 5 presents our investigation into vacancy migration in monolayer SiC using nudged elastic band (NEB) calculations, employing the HSE06 functional with D3 dispersion correction. Figures 5(a) and 5(b) illustrate the top view of the monolayer SiC structure, showing the migration pathways for Si and C vacancies, respectively. For both vacancy types, we considered three distinct pathways: Path A (green) involves migration to the diagonal position of the same atom type within a single hexagon, Path B (pink) represents migration to the same atom type position diagonally crossing two hexagons, and Path C (blue) depicts migration to the nearest neighbor of the same atom type. The energy profiles along these

migration pathways for Si vacancies (Fig. 5c) and C vacancies (Fig. 5d) reveal significant differences in migration barriers. For Si vacancies, Path C exhibits the lowest energy barrier of 0.38 eV, making it the most favorable migration route. Path A presents an intermediate barrier of 1.12 eV, while Path B has the highest barrier of 1.41 eV, making it the least likely route for Si vacancy migration. Similarly, for C vacancies, Path C again presents the lowest energy barrier at 0.81 eV, followed by Path A with 1.33 eV and Path B with 1.76 eV. These results indicate that migration to the nearest neighbor (Path C) is energetically favored for both Si and C vacancies, while migration across two hexagons (Path B) is the least likely. Notably, the energy barriers for C vacancies are consistently higher than those for Si vacancies across all pathways, suggesting that C vacancies are less mobile and more stable in the 1L-SiC lattice. The lower energy barriers for Path C can be attributed to its shorter migration distance and the preservation of the local bonding environment. In contrast, Path B involves significant bond breaking and reforming over a longer distance, leading to higher energy barriers. Path A represents an intermediate case, requiring some bond rearrangement but over a shorter distance compared to Path B. Examination of the transition state (TS) configurations provides further insights into the atomic-scale mechanisms of vacancy migration. For both vacancy types, the TS for Path C involves a displacement of the migrating atom towards the vacancy site by approximately 0.8 Å, with a slight out-of-plane distortion of about 0.2 Å. This minimal distortion contributes to the lower energy barrier for this path. In contrast, the TS for Path B shows significant in-plane lattice distortion, with neighboring atoms displaced by up to 0.5 Å, and out-of-plane buckling of up to 0.4 Å, consistent with its higher energy barrier. Interestingly, the energy difference between the initial state (IS) and final state (FS) for each migration pathway is relatively small (less than 0.1 eV), indicating that the vacancies do not have a strong preference for specific lattice sites. This suggests that vacancy movement in monolayer SiC is primarily influenced by kinetic factors rather than thermodynamic considerations. It's important to note that our calculations consider only neutral vacancies. The migration behavior of charged vacancies may differ significantly due to changes in the local electronic structure and lattice relaxation. While we can speculate that positively charged vacancies might exhibit lower migration barriers due to reduced electron density in the defect region, and negatively charged vacancies might have higher barriers due to increased electron-electron repulsion, these predictions are purely speculative and would require further computational validation to confirm. The comparison with bulk SiC provides valuable context for understanding the unique properties of defects in 2D SiC. In 3C-SiC, for example, Si vacancy migration barriers have been reported to be around 3.5-5.2 eV [57, 58], significantly higher than our predicted value of 0.38 eV for 1L-SiC. These theoretical predictions of

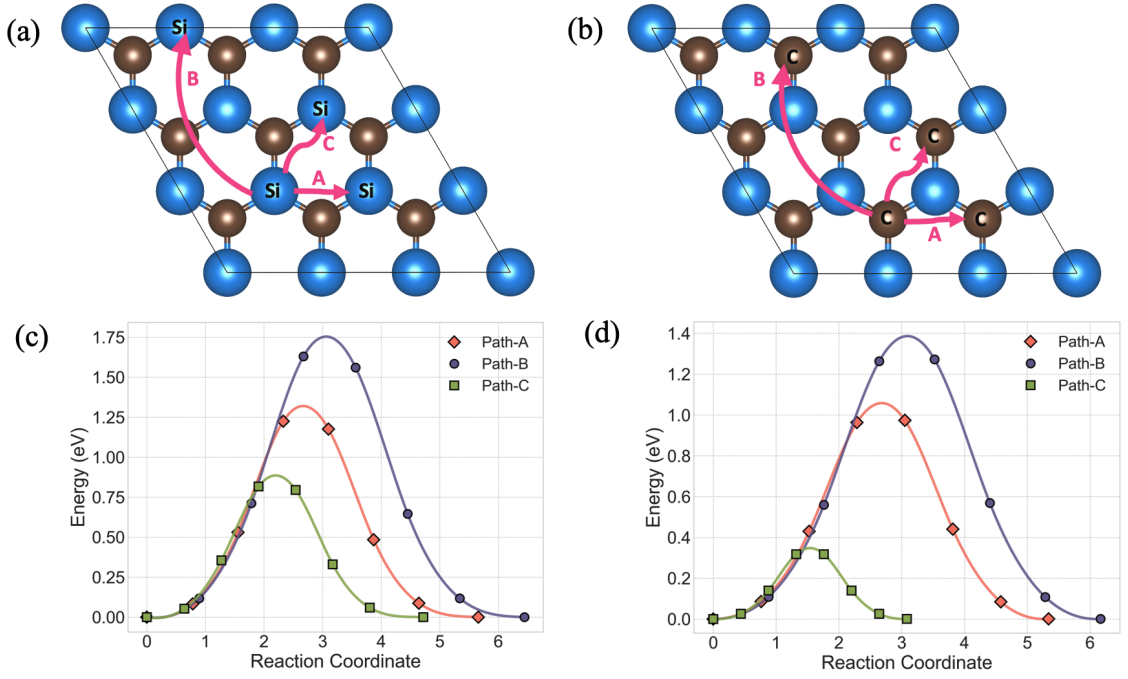


FIG. 5. Nudged elastic band (NEB) calculations of silicon and carbon vacancy migration pathways in 1L-SiC using the HSE06 functional with D3 dispersion correction.

vacancy migration are particularly relevant given recent experimental demonstrations of 2D SiC synthesis. Chemical exfoliation methods have shown that 2D SiC is stable under ambient conditions [30], while epitaxial growth has demonstrated stability up to 1200°C in vacuum [31]. The predicted migration barriers help explain this remarkable thermal stability, though substrate effects may further modify defect dynamics in experimental samples.

D. Optical Properties

The introduction of vacancies in monolayer SiC (1L-SiC) induces profound changes in its optical properties, as revealed by our calculations of the dielectric function and absorption coefficient. Figure 6 presents a comprehensive analysis of the real (ϵ_1) and imaginary (ϵ_2) parts of the dielectric function (Figures 6a and 6c), as well as the corresponding optical absorptivity (Figures 6b and 6d), computed using the PBE functional within DFPT formalism. While HSE06 was used for electronic structure calculations, optical properties were computed using PBE-DFPT due to its established reliability in predicting optical response functions and significantly lower computational cost for excited state properties, following the approach validated by Lan et al. [59]. For pristine 1L-SiC, ϵ_2 exhibits a prominent peak at approximately 4 eV, corresponding to fundamental optical transitions across the bandgap, in agreement with previous theoretical predictions [60]. The real part of the dielectric function (ϵ_1)

shows a characteristic oscillator-like behavior, with its magnitude directly influencing the material's refractive index. The relationship between these dielectric components and the absorption coefficient (α) can be expressed through:

$$\alpha = \frac{4\pi k}{\lambda} \quad (4)$$

, where

$$k = \sqrt{\frac{\sqrt{\epsilon_1^2 + \epsilon_2^2} - \epsilon_1}{2}} \quad (5)$$

. The introduction of silicon vacancies (V_{Si}) dramatically modifies these optical responses, particularly in the low-energy region (0-0.5 eV). For the neutral silicon vacancy (V_{Si}^0), a distinct peak emerges at approximately 0.05 eV in both ϵ_1 and ϵ_2 , with ϵ_2 reaching a value of about 18. This peak position aligns well with recent experimental observations of defect-induced optical transitions in chemically exfoliated 2D SiC [30], and the large ϵ_2 value is consistent with the strong excitonic effects predicted by Lan et al. [59]. The correlation between electronic structure and optical transitions is particularly evident here, as these low-energy features correspond directly to the defect states observed in Figure 3a. The negatively charged silicon vacancy (V_{Si}^{-1}) exhibits a broad response in both ϵ_1 and ϵ_2 below 0.1 eV, with ϵ_2 showing multiple peaks of magnitude around 5. This electronic structure results in enhanced absorption in the far-infrared region,

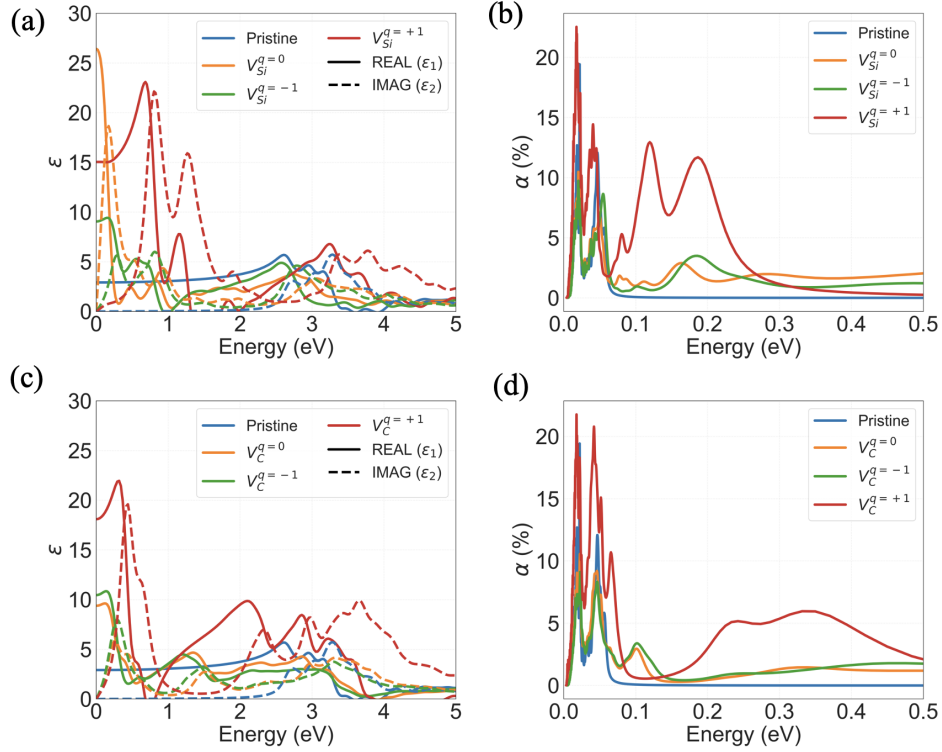


FIG. 6. Optical properties of vacancy defects in 1L-SiC computed using PBE-DFPT: (a,c) Real (ϵ_1 , solid lines) and imaginary (ϵ_2 , dashed lines) parts of the dielectric function for Si and C vacancies respectively in different charge states. The pristine case is shown in blue for reference. (b,d) Corresponding absorption coefficients (α) shown as percentage change relative to pristine SiC. The low-energy region (0-0.5 eV) exhibits the strongest vacancy-induced features, with distinct absorption characteristics for each charge state.

with the absorption coefficient showing peaks of approximately 8-9% at energies below 0.1 eV, comparable to the absorption features observed in other 2D semiconductors with charged defects [31]. These features can be directly correlated with the multiple transitions available between the spin-split states observed in the electronic structure calculations. For the positively charged silicon vacancy (V_{Si}^{+1}), the dielectric response is particularly strong, with ϵ_2 showing distinctive peaks reaching values above 20 at around 0.1 eV. This enhanced dielectric response translates into the highest absorption among all vacancy states, with the absorption coefficient reaching approximately 22% at low energies and showing multiple strong absorption bands between 0.1-0.3 eV. The strong absorption in this charge state can be attributed to the asymmetric electronic structure revealed in Figure 3c, where the presence of both localized and metallic states enables multiple optical transitions. The carbon vacancy optical response shows systematic evolution with charge state, as shown in Figures 6c and 6d. For the neutral carbon vacancy (V_C^0), the moderate peaks in ϵ_2 (~ 5) translate to absorption coefficients of 3-4%, reflecting the relatively weak oscillator strength of transitions between the delocalized defect states. V_C^{-1} exhibits enhanced absorption (5-6%) due to additional transitions enabled

by the extra electron, while V_C^{+1} shows the strongest response with ϵ_2 reaching ~ 20 at energies below 0.05 eV. This pronounced increase in oscillator strength for V_C^{+1} results in absorption peaks exceeding 20%, making it particularly promising for far-infrared optoelectronic applications. The contrasting optical behavior of Si and C vacancies can be understood through their distinct electronic structures, a phenomenon also observed in recent experimental studies [30]. Si vacancies create highly localized states leading to sharp optical transitions, while C vacancies produce more dispersed states resulting in broader absorption features. This difference is particularly evident in the positively charged state, where V_{Si}^{+1} shows discrete absorption bands between 0.1-0.3 eV, while V_C^{+1} exhibits a more continuous absorption profile extending up to 0.4 eV. Our predictions are further supported by recent experimental demonstrations of substrate-dependent optical properties in epitaxially grown 2D SiC [31], which suggest that the optical response can be modified through environmental effects. The strong charge-state dependence of optical properties aligns with theoretical predictions by Lan et al. [59] regarding excitonic effects in 2D SiC, particularly the enhancement of absorption strength through charge state modification. The magnitude of enhancement we predict

(up to 22% for $V_{Si/C}^{+1}$) is notably higher than in other 2D materials, suggesting unique opportunities for optoelectronic applications. Recent experimental validation comes from photoluminescence measurements on chemically exfoliated 2D SiC showing visible light emission [30], consistent with our predicted optical transitions. The observed quantum confinement effects highlighted in comprehensive reviews [61] support our predictions of enhanced absorption and excitonic effects compared to bulk SiC. Furthermore, the strain-dependent optical properties reported by Lin et al. [60] suggest additional possibilities for tuning these optical responses through mechanical deformation. These findings open new avenues for developing tunable far-infrared optical devices based on charged vacancy states in 2D SiC. The complementary absorption characteristics of silicon and carbon vacancies, combined with their strong charge-state dependence, suggest possibilities for electrostatically controlled optical devices operating in the far-infrared regime, with potential applications ranging from photodetectors to optical modulators.

IV. CONCLUSIONS

This comprehensive study of silicon and carbon vacancies in monolayer SiC (1L-SiC) using density functional theory (DFT) has provided crucial insights into the electronic, structural, and optical properties of these defects. Our investigation, employing a range of exchange-correlation functionals (PBE, SCAN, r²SCAN, and HSE06) and charge correction schemes (FNV and KO), demonstrates the critical importance of methodology in accurately predicting defect properties in 2D materials. The formation energies of silicon and carbon vacancies reveal significant variations across functionals, with HSE06 consistently predicting the highest values, highlighting the substantial impact of exact exchange inclusion on defect energetics. The electronic structure analysis demonstrates distinct characteristics between silicon and carbon vacancies. Silicon vacancies introduce highly localized defect states, with HSE06 calculations revealing strong spin polarization effects and a gap of approximately 2 eV for spin-up states. In contrast, carbon vacancies exhibit more dispersed states with broader bandwidth (0.5 eV), suggesting stronger orbital overlap with neighboring atoms. The progression of electronic structure across charge states shows intriguing magnetic behavior, particularly evident in HSE06 calculations, where spin polarization persists even in charged states. Migration pathway analysis reveals significantly lower barriers for silicon vacancies (0.38 eV) compared to carbon vacan-

cies (0.81 eV), indicating higher mobility of silicon vacancies at moderate temperatures. This finding has important implications for defect dynamics and the potential formation of vacancy complexes in 1L-SiC. Our optical property calculations using PBE-DFPT reveal significant modifications to the dielectric response and absorption characteristics, particularly in the far-infrared region (0-0.5 eV). Positively charged vacancies demonstrate the strongest optical response, with absorption coefficients reaching 22%. The distinct behavior of silicon and carbon vacancies - with silicon vacancies showing sharp, discrete absorption features and carbon vacancies exhibiting broader absorption profiles - provides complementary functionalities for potential optoelectronic applications. The choice of computational methodology proves crucial for accurate predictions. While HSE06 provides the most reliable results for electronic structure and energetics, the computational efficiency of meta-GGA functionals like SCAN and r²SCAN makes them attractive for initial screening studies. The PBE-DFPT approach demonstrates reliability for optical property calculations while maintaining computational efficiency. These findings open several promising directions for future research. The strong charge-state dependence of optical properties suggests possibilities for electrostatically tunable optical devices operating in the far-infrared region. The distinct characteristics of silicon and carbon vacancies could be exploited for dual-functionality devices combining sharp, state-specific optical transitions with broader absorption bands. Future work should focus on exploring the interplay between different types of defects, investigating strain effects on defect properties, and experimental validation of these theoretical predictions. This work establishes a comprehensive framework for investigating defects in 2D materials and demonstrates how careful selection of computational methods can provide detailed insights into defect properties. The complementary functionalities of silicon and carbon vacancies revealed in this study suggest exciting possibilities for defect engineering in next-generation quantum and optoelectronic devices based on 2D SiC.

V. AUTHOR CONTRIBUTIONS

A. Patra conceived the study, performed calculations, and wrote the manuscript.

VI. CONFLICTS OF INTEREST

There are no conflicts to declare.

[1] A. L. Falk, P. V. Klimov, V. Ivady, K. Szasz, D. J. Christle, W. F. Koehl, A. Gali, and D. D. Awschalom, *Nature*

Communications **6**, 1 (2015).

- [2] R. Nagy, M. Widmann, M. Niethammer, D. B. Dasari, I. Gerhardt, O. O. Soykal, M. Radulaski, T. Ohshima, J. Vučković, N. T. Son, *et al.*, *Nature Communications* **10**, 1 (2019).
- [3] G. Wolfowicz, S. J. Whiteley, and D. D. Awschalom, *New Journal of Physics* **23**, 023021 (2021).
- [4] P. Baranov, A. Bundakova, A. Soltamova, S. Orlinskii, I. Borovykh, R. Zondervan, R. Verberk, and J. Schmidt, *Physical Review B* **83**, 125203 (2011).
- [5] D. Riedel, F. Fuchs, H. Kraus, S. V'ath, A. Sperlich, V. Dyakonov, A. A. Soltamova, P. G. Baranov, V. A. Ilyin, and G. V. Astakhov, *Physical Review Letters* **109**, 226402 (2012).
- [6] K. Sz'asz, V. Iv'ady, I. A. Abrikosov, E. Janz'en, M. Bockstedte, and A. Gali, *Physical Review B* **88**, 075202 (2013).
- [7] S. Castelletto, B. Johnson, V. Iv'ady, N. Stavrias, T. Umeda, A. Gali, and T. Ohshima, *Nature materials* **13**, 151 (2014).
- [8] D. J. Christle, A. L. Falk, P. Andrich, P. V. Klimov, J. U. Hassan, N. T. Son, E. Janz'en, T. Ohshima, and D. D. Awschalom, *Nature Materials* **14**, 160 (2015).
- [9] M. Radulaski, M. Widmann, M. Niethammer, J. L. Zhang, S.-Y. Lee, T. Rendler, K. G. Lagoudakis, N. T. Son, E. Janz'en, T. Ohshima, *et al.*, *Nano Letters* **17**, 1782 (2017).
- [10] J. Davidsson, V. Iv'ady, R. Armiento, T. Ohshima, N. T. Son, A. Gali, and I. A. Abrikosov, *New Journal of Physics* **20**, 023035 (2018).
- [11] J. Davidsson, V. Iv'ady, R. Armiento, T. Ohshima, N. Son, A. Gali, and I. A. Abrikosov, *Applied Physics Letters* **114** (2019).
- [12] A. Gali, J. R. Maze, M. E. Trusheim, L. M'ark, G. Barcza, and V. Ivady, *npj Computational Materials* **5**, 1 (2019).
- [13] P. Udvarhelyi, V. O. Shkolnikov, A. G'ali, G. Burkard, and A. P'alyi, *npj Computational Materials* **6**, 1 (2020).
- [14] T. Kobayashi, K. Harada, Y. Kumagai, F. Oba, and Y.-i. Matsushita, *Journal of Applied Physics* **125** (2019).
- [15] A. J. Islam, M. S. Islam, N. Ferdous, J. Park, and A. Hashimoto, *Physical Chemistry Chemical Physics* **22**, 13592 (2020).
- [16] J. Fan, X. Wu, and P. K. Chu, *Progress in materials science* **51**, 983 (2006).
- [17] K. Yamasue, H. Fukidome, K. Funakubo, M. Suemitsu, and Y. Cho, *Physical Review Letters* **114**, 226103 (2015).
- [18] N. Mishra, S. Jain, J. R. Panigrahi, H. Pathak, S. Kale, and A. Pramanik, *Ceramics International* **42**, 16297 (2016).
- [19] V. A. Volodin, A. A. Gismatulin, V. A. Gritsenko, G. Y. Krasnikov, and A. V. Palagin, *Materials* **11**, 756 (2018).
- [20] N. Nilius, T. Wallis, and W. Ho, *Science* **297**, 1853 (2002).
- [21] F. Fuchs, B. Stender, M. Trupke, D. Simin, J. Pflaum, V. Dyakonov, and G. Astakhov, *Nature communications* **6**, 7578 (2015).
- [22] N. B. Manson, M. W. Doherty, and L. C. Hollenberg, *Physical Review B* **94**, 155203 (2016).
- [23] M. Bockstedte, F. Sch'utz, T. Garratt, V. Iv'ady, and A. Gali, *npj Quantum Materials* **3**, 1 (2018).
- [24] W. F. Koehl, B. B. Buckley, F. J. Heremans, G. Burkard, and D. D. Awschalom, *Nature* **556**, 368 (2018).
- [25] M. Radulaski, J. L. Zhang, Y.-K. Tzeng, K. G. Lagoudakis, H. Ishiwata, C. Dory, K. A. Fischer, Y. A. Kelaita, S. Sun, P. C. Maurer, K. Alassaad, G. Ferro, Z.-X. Shen, N. A. Melosh, S. Chu, and J. Vučković, *Laser & Photonics Reviews* **13**, 1800316 (2019).
- [26] Z.-D. Wang, Y. Abe, J. Lang, J. Qian, T. Ohshima, W. Ya-Dong, J. Zi-Yuan, W. Dong-Ping, Z. Jian-Qi, C. Kai-Mei, *et al.*, *Physical Review Applied* **13**, 064006 (2020).
- [27] M. Pizzochero, C. Berthod, M. Pizzochero, and C. Berthod, *Journal of Applied Physics* **126**, 145702 (2019).
- [28] P. Udvarhelyi, G. Thiering, N. Morioka, C. Babin, F. Kaiser, D. Lukin, T. Ohshima, J. Ul-Hassan, N. T. Son, J. Vucković, *et al.*, *Physical Review Applied* **13**, 054017 (2020).
- [29] P. Abellan, D. Akbarian, A. Alieva, T. Altantzis, T. S. Andersen, M. E. R. Arenal, S. Arunachalam, J. Azpeitia, R. Bachelet, *et al.*, *2D Materials* **8**, 042003 (2021).
- [30] S. Chabi, Z. Guler, A. J. Brearley, A. D. Benavidez, and T. S. Luk, *Nanomaterials* **11**, 1799 (2021).
- [31] C. Polley, H. Fedderwitz, T. Balasubramanian, A. Zakharov, R. Yakimova, O. B'acke, J. Ekman, S. Dash, S. Kubatkin, and S. Lara-Avila, *Physical Review Letters* **130**, 076203 (2023).
- [32] J. P. Perdew, K. Burke, and M. Ernzerhof, *Physical Review Letters* **77**, 3865 (1996).
- [33] Y. Zhang and W. Yang, *Physical Review Letters* **80**, 890 (1998).
- [34] C. Adamo and V. Barone, *The Journal of Chemical Physics* **110**, 6158 (1999).
- [35] J. Heyd, G. E. Scuseria, and M. Ernzerhof, *The Journal of chemical physics* **118**, 8207 (2003).
- [36] A. V. Krukau, O. A. Vydrov, A. F. Izmaylov, and G. E. Scuseria, *The Journal of chemical physics* **125** (2006).
- [37] J. Paier, M. Marsman, and G. Kresse, *The Journal of chemical physics* **127** (2007).
- [38] J. Sun, A. Ruzsinszky, and J. P. Perdew, *Physical Review Letters* **115**, 036402 (2015).
- [39] J. Sun, R. C. Remsing, Y. Zhang, Z. Sun, A. Ruzsinszky, H. Peng, Z. Yang, A. Paul, U. Waghmare, X. Wu, *et al.*, *Nature Chemistry* **8**, 831 (2016).
- [40] J. W. Furness, Y. Zhang, C. Lane, I. G. Buda, B. Barbiellini, R. S. Markiewicz, A. Bansil, and J. Sun, *Communications Physics* **3**, 1 (2020).
- [41] Y.-H. Zhang, H. Peng, H. Ma, J. W. Furness, J. Sun, and J. P. Perdew, *Physical Review Letters* **127**, 176402 (2021).
- [42] G. Kresse and J. Furthm'uller, *Physical review B* **54**, 11169 (1996).
- [43] P. E. Bl'ochl, *Physical review B* **50**, 17953 (1994).
- [44] J. P. Perdew, K. Burke, and M. Ernzerhof, *Physical review letters* **77**, 3865 (1996).
- [45] J. Sun, A. Ruzsinszky, and J. P. Perdew, *Physical Review Letters* **115**, 036402 (2015).
- [46] J. W. Furness, A. D. Kaplan, J. Ning, J. P. Perdew, and J. Sun, *The journal of physical chemistry letters* **11**, 8208 (2020).
- [47] J. Heyd, J. E. Peralta, G. E. Scuseria, and R. L. Martin, *The Journal of chemical physics* **123** (2005).
- [48] E. Caldeweyher, C. Bannwarth, and S. Grimme, *The Journal of chemical physics* **147** (2017).
- [49] H. J. Monkhorst and J. D. Pack, *Physical review B* **13**, 5188 (1976).
- [50] G. Henkelman and H. J'onnsson, *The Journal of chemical physics* **113**, 9978 (2000).

- [51] C. Freysoldt, J. Neugebauer, and C. G. Van de Walle, *Physical review letters* **102**, 016402 (2009).
- [52] Y. Kumagai and F. Oba, *Physical Review B* **89**, 195205 (2014).
- [53] T.-Y. Lü, X.-X. Liao, H.-Q. Wang, and J.-C. Zheng, *Journal of Materials Chemistry* **22**, 10062 (2012).
- [54] C. V. Ha, D. K. Nguyen, D. T. Anh, J. Guerrero-Sanchez, and D. Hoat, *New Journal of Chemistry* **47**, 2787 (2023).
- [55] M. Mohseni, I. A. Sarsari, S. Karbasizadeh, P. Udvarhelyi, Q. Hassanzada, T. Ala-Nissila, and A. Gali, *Physical Review Materials* **8**, 056201 (2024).
- [56] E. Bekaroglu, M. Topsakal, S. Cahangirov, and S. Ciraci, *Physical Review B* **81**, 075433 (2010).
- [57] M. Bockstedte, A. Mattheis, and O. Pankratov, *Physical Review B* **68**, 205201 (2003).
- [58] F. Gao, W. J. Weber, M. Posselt, and V. Belko, *Physical Review B—Condensed Matter and Materials Physics* **69**, 245205 (2004).
- [59] Y.-Z. Lan, *Computational Materials Science* **138**, 213 (2017).
- [60] X. Lin, S. Lin, Y. Xu, A. A. Hakro, T. Hasan, B. Zhang, B. Yu, J. Luo, E. Li, and H. Chen, *Journal of Materials Chemistry C* **1**, 2131 (2013).
- [61] S. Chabi and K. Kadel, *Nanomaterials* **10**, 2226 (2020).